Nanoscale

ROYAL SOCIETY
OF **CHEMISTRY**

PAPER
Rafik Naccache *et al.*
Response surface analysis of CuInSe₂ nanoparticle synthesis:
unravelling the interplay of temperature, time, and ligand
composition for size control

NCNST

PAPER

Check for updates

Response surface analysis of CuInSe₂ nanoparticle synthesis: unravelling the interplay of temperature, time, and ligand composition for size control

Luis Páramo, [a,b] Camilo Garcia-Henao, [ID] [a,b] John A. Capobianco [ID] [a,b] and Rafik Naccache [ID] *[a,b]

CuInSe₂ nanoparticles are promising materials for solar energy conversion owing to their broad and tunable optical absorption and the absence of heavy metals such as cadmium or lead. However, current synthesis methods for ternary chalcogenides are largely constrained by inefficient one-variable-at-a-time strategies, limiting the understanding of how reaction parameters and their interactions influence nanoparticle properties. Here, we apply a statistical approach based on a Box–Behnken response surface model to evaluate the influence of temperature (200–240 °C), reaction time (5–10 min), and ligand composition defined by different oleylamine/oleic acid volume combinations (1/3, 2/2, and 3/1 mL) on nanoparticle average size which varied from 7.3 to 15.4 nm depending on synthesis conditions. Statistical analysis showed that all three variables were significant ($p < 0.05$), with temperature having the strongest influence, achieving a predicted R^2 of 0.85. Oleylamine-rich conditions favored smaller nanoparticles (~12.5 nm), whereas oleic-acid-rich mixtures produced larger ones (~15 nm) at 240 °C. Interactions among temperature, time, and ligand composition also revealed variations in growth rate resulting from the combined effects of these variables. Representative conditions from the model were then selected to study how ZnS passivation affects photoluminescence. Among these, samples synthesized at 200 °C showed the most intense emission, particularly under oleic-acid-rich conditions, suggesting that low temperature and higher oleic acid content promote more effective surface passivation and radiative recombination. This statistical approach can be extended to other chalcogenide systems that share similar synthesis conditions, allowing the systematic study of multiple variables at once. By showing how synthesis factors and their interactions influence average size and surface characteristics, it provides a predictive basis for more controlled nanoparticle design.

Introduction

Copper chalcogens, such as CuIn(S/Se)₂, have recently come to light as sustainable alternatives to heavy metal-based chalcogenides (*e.g.* CdS, CdSe) for applications in sensing, catalysis, and solar energy conversion, owing in part to their heavy metal-free composition, without the requirement for toxic metals such as Pb and Cd.[1–4] In addition, the ternary chalcogenides are particularly interesting in solar energy conversion with optical properties that include high absorption coefficients extending to the infrared regions.[5] Their optical properties can be tuned through various strategies, such as adjust-

ing the nanocrystal size, changing the chalcogen element ratio (S/Se) in mixed compositions, or altering the metal concentration ratio (Cu/In). These approaches make them promising candidates for precisely tailoring absorption across different wavelength ranges.[5–7] However, unlike binary structures (*e.g.*, CdS, CdSe, CuSe, CuS), whose synthesis has been extensively studied, achieving precise control over the morphology and optical properties of ternary systems remains a significant challenge. The control of their properties critically depends on the reaction conditions, requiring a delicate balance between precursor reactivity, to avoid forming binary phases, and controlling the composition stoichiometry.[8,9]

Currently, the most common approach for synthesising CuIn(S/Se)₂ nanomaterials, or quantum dots, involves using hot injection methodologies.[6,10–13] Parameters such as temperature, reaction time, ligand selection, and the composition of solvents play a strategic role in defining the material's resultant properties.[14–17] For example, according to the hard and

*[a]Department of Chemistry and Biochemistry and the Centre for NanoScience Research, Concordia University, Montreal, Quebec H3G 1M8, Canada.
E-mail: rafik.naccache@concordia.ca
[b]Quebec Centre for Advance Materials, Concordia University, Montreal, Quebec H3G 1M8, Canada*

soft acid–base theory, ligand mixtures can affect the reactivity of the metal precursors, impacting reaction rates, colloidal stability, and morphological control.[18] Temperature and time can also affect nanocrystal size and crystalline quality, both of which are critical parameters in $CuIn(S/Se)_2$ systems as the photoluminescent properties of these materials are closely linked to the presence and nature of structural defects.[19–22]

Typically, when studying multiple factors in a synthesis, the process begins by assessing the impact of the first factor and selecting the most appropriate value based on the desired property. This value is then fixed while the next factor is changed, and the procedure is repeated until the "optimal" combination of values for all factors is determined. This method is commonly known as one variable at a time (OVAT), which limits our understanding of variable effects and the relationship, or interplay, between multiple factors in a synthesis. In this way, using OVAT, it is not possible to explain a relation between the various variables, which, through their interaction, may offer better conditions than an isolated factor optimisation paradigm. Depending on the precision desired, OVAT may require more experiments to achieve an optimal value, slowing down research in exchange for poor knowledge about reaction dynamics.[23–27]

Strategies such as the design of experiments (DOE) and response surface analysis (RSA) allow the identification of relevant factors and interactions (linear or non-linear) and optimize synthesis conditions in search of property tuning to address the disadvantages of OVAT.[27] Both types of analysis will enable the study of multiple factors, aiding in identifying linear and nonlinear interactions. Statistical analysis allows for determining their significance, eliminating variables that may not be important in modifying sought after properties, and reducing the overall number of experiments.[23,27] This is relevant in nanoparticle (NPs) synthesis, which often requires expensive precursors that may limit the scope of property tuning and scalability. In the NPs synthesis field, these techniques allow researchers to glean a better understanding of the relationship between factors necessary for their synthesis, improving the control and quality of the synthesized materials.[25,27] Another advantage of this model is the possibility of knowledge transferability, where the observed factor importance can be translated to similar compositions that share identical or equal synthesis paths (e.g. $CuInGa(S/Se)_2$).

Several recent studies have applied experimental design and RSA to identify critical experimental parameters on factors such as quantum yield,[28,29] NPs size,[24,26,30] emission intensity,[31,32] emission band position,[25] reaction yields,[23,24,33] and band gap,[34] offering suitable results for predicting and optimising these properties, as well as improving rational synthesis design. To date, DOE or RSA approaches in the ternary copper chalcogenide family have only been explored in $CuAlS_2$ NPs to analyse photoluminescence properties.[32] However, their use for the synthesis of $CuIn(S/Se)_2$ quantum dots remains relatively unexplored, which opens the opportunity to establish reproducible and efficient methodologies for their production. Given the technological relevance of these

materials, it is essential to employ strategies that clarify the roles of key variables to enable their effective integration in applications.

Herein, this study aims to evaluate the effect of three synthesis parameters namely temperature (200, 220, and 240 °C), ligand composition defined by different oleylamine/oleic acid volume combinations (1/3, 2/2, and 3/1 mL), and reaction time (5, 17.5, and 30 min) on the average size of $CuInSe_2$ NPs synthesized through the hot-injection method. These parameters were chosen because they are known to strongly influence nucleation and growth in colloidal synthesis and can be changed without altering precursor chemistry. A Box–Behnken RSA was implemented and fitted to a quadratic model, using the mean particle size (measured via transmission electron microscopy, TEM) as the response. Following the RSA, ZnS passivation was performed under selected conditions to identify variable combinations associated with improved optical properties. Overall, this work provides a statistical framework to relate synthesis variables with particle size and photoluminescence response, offering practical guidance for tailoring $CuInSe_2$-based nanomaterials for optoelectronic applications.

Experimental section

Materials

Copper(I) iodide (CuI, 98%), selenium powder (−100 mesh, ≥99.5% trace metals basis), hexane (≥98.5%, mixture of isomers), ethanol (≥99%), oleylamine (OAm, 70% technical grade), oleic acid (Oa, 90% technical grade), 1-octadecene (ODE, 90% technical grade), and zinc stearate ($Zn(St)_2$, technical grade) were obtained from Sigma-Aldrich and used as received. Indium(III) chloride anhydrous ($InCl_3$, 98+% trace metals basis) and 1-dodecanethiol (DDT, 98%) were purchased from Thermoscientific and used as received.

Synthesis of $CuInSe_2$ NPs

The synthesis of $CuInSe_2$ was performed following the protocol in the work of Lian et al. (2020)[2] with slight modifications, as shown in Fig. 1a. In a 3-neck round-bottom flask labelled A, 0.4 mmol of CuI and 0.4 mmol of $InCl_3$ were placed along with 16 mL of octadecene and a magnetic stirrer. Flask A was placed over a heating mantle, and the neck was closed using a rubber septum and a vacuum adapter; a temperature sensor was also placed on one septum. The solution was purged with argon for 5 min. Subsequently, a specific amount of OAm(mL)/Oa(mL) was added based on the RSA design (1/3, 2/2, 3/1), resulting in 4 mL of ligands in the mixture of flask A. The temperature was then increased to 120 °C, while a vacuum was started at that temperature for 30 min. The temperature was then raised to the target values of 200 °C, 220 °C, or 240 °C. A separate solution, labelled B, was prepared in a scintillation vial by placing 0.8 mmol of elemental Se and a mixture of 0.6 mL DDT along with 1.4 mL of Oam were it was placed in agitation until the complete dissolution of Se. This Se solution
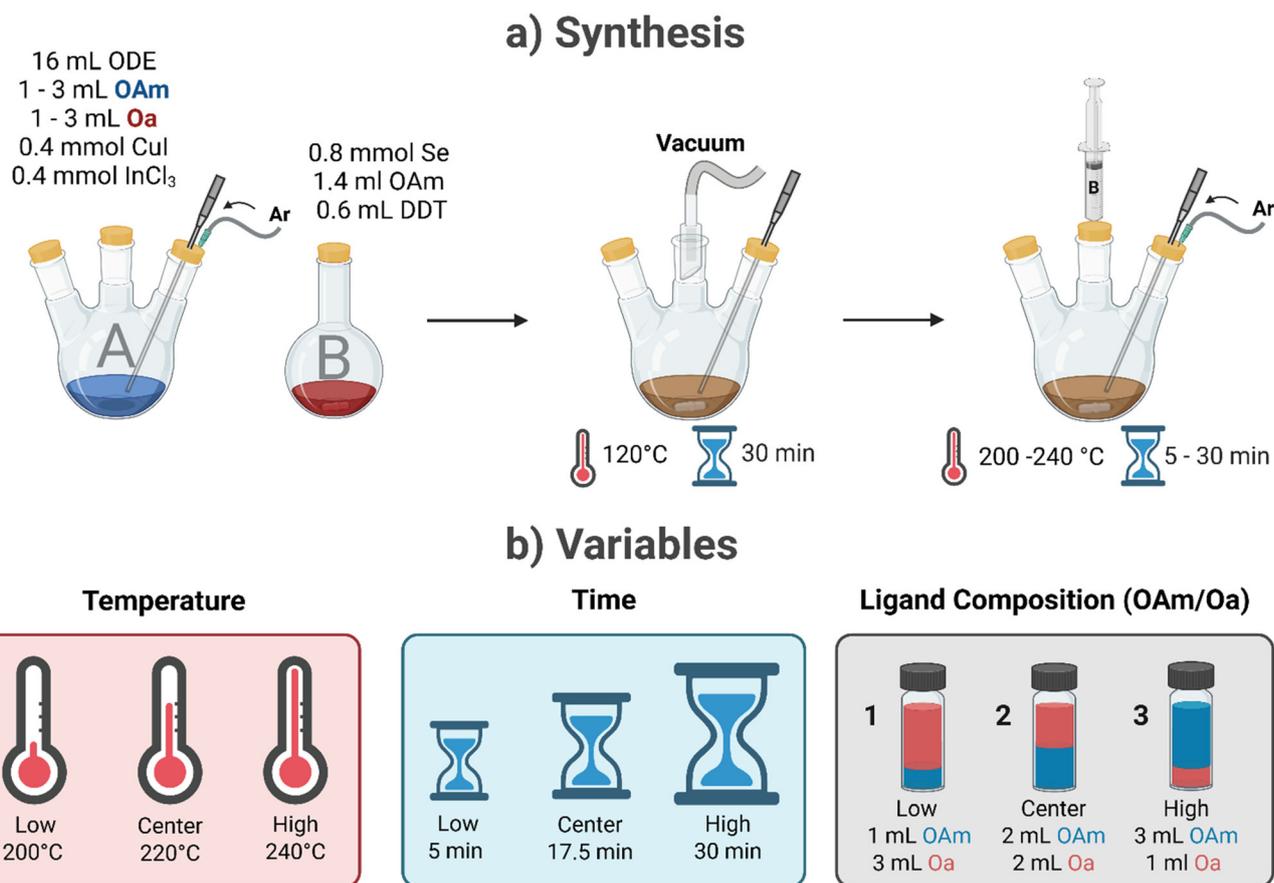
a) Synthesis

b) Variables

Fig. 1 (a) Variables selected for the construction of the RSA: temperature range was set from 200 °C (low) to 240 °C (high), with the center point at 220 °C. Time range was selected from 5 minutes (low) to 30 minutes (high), with the center point at 17.5 minutes. Ligand composition was adjusted by varying the added volumes of oleylamine and oleic acid: 1 mL OAm + 3 mL OA for the low end (1), 2 mL OAm + 2 mL Oa for the center point (2), and 3 mL OAm + 1 mL Oa for the high end (3).

was rapidly injected into flask A once the desired temperature had been reached. The reaction was allowed to continue for a selected period of time, namely 5, 17.5, or 30 min. At the end of the reaction, flask A was removed from the heating mantle and it was allowed to cool down to room temperature. The sample was then purified by precipitation with anhydrous ethanol, followed by centrifugation at 10 000g for 5 min. The supernatant was discarded, and the product was redispersed in hexane with the purification process repeated two additional times. Finally, the samples were redispersed in hexane prior to analysis and passivation.

ZnS passivation

ZnS passivation was carried out following the protocol reported in the work of Lian *et al.* (2020)[2] with slight modifications, where a solution of 40 mg mL^{-1} of the CuInSe$_2$ NPs, in hexane, was added to a 3-neck round-bottom flask containing 0.2 mmol of Zn(St)$_2$, 5 mL of ODE, 0.5 mL of OAm, and 0.3 mL of Oa under vigorous stirring. The mixture was purged with Ar, and the temperature was raised to 120 °C, where it was subjected to a vacuum for 30 min to eliminate water traces and hexane. Subsequently, the mixture was purged again with Ar and heated

to 200 °C. 0.5 mL of DDT was introduced to the flask using a syringe pump over 20 minutes. Finally, the product was cooled to room temperature and subjected to solvent washes as previously described before redispersing the mixture in hexane.

Response surface analysis

OriginPro 2023b (10.0.5.157) was used to construct and analyse the RSA using the DOE app. A Box–Behnken design with three factors was selected, considering temperature (200–240 °C), reaction time (5–30 min), and OAm/Oa volume (1/3, 2/2, 3/1), whose values were imputed as (1, 2, 3), the experimental variable ranges and their corresponding coded values are summarized in Table S1. Three replicates at the centre point were included to estimate pure error and validate the model. The selected responses based on the TEM data were the average particle size and standard deviation. Experimental runs were randomized to minimize systematic error, and model significance was assessed using analysis of variance (ANOVA) and lack-of-fit tests provided by the OriginPro DOE app. Response values were fitted to a full quadratic model with a confidence value of 95%. The Percentage of Contribution (%C) was calculated to quantify the influence of

each variable using the following formula where SS_V is the sum of squares of an individual variable and SS_T is the total sum of squares from the ANOVA table (Table 1).

$$\%C = \left(\frac{SS_V}{SS_T}\right)100$$

Transmission electron microscopy (TEM)

TEM was performed using a Thermo Fisher Talos L120C microscope operated at 120 kV. Samples were prepared by drop-casting a diluted dispersion of the quantum dots in hexane onto carbon-coated copper grids (300 mesh), allowing them to dry under ambient conditions. TEM micrographs were acquired in multiple random fields of view. Size distributions were obtained by measuring a range between 80 and 100 particles using the ImageJ software and reporting the average ± standard deviation.

UV-Vis spectroscopy (UV-Vis)

Optical absorption spectra were recorded using an Agilent Cary 5000 UV-Vis spectrophotometer. Measurements were carried out in the 200–800 nm range at a concentration of 5 mg mL^{-1}.

Photoluminescence spectroscopy (PL)

Photoluminescence (PL) measurements were performed on a FERGIE BRX-VR UV-NIR spectrograph (Princeton Instruments). A detector collected the emission spectra in the 700–1100 nm range. Samples were excited using a light source with a peak emission at 365 nm. The emission was collected using a 1500 μm, 0.5 numeric aperture, low OH spectrograph purchased from Thor Labs. Prior to analysis, NPs samples were dispersed in hexane at a concentration of 5 mg mL^{-1}.

Near infrared photography

Near infrared photographs were taken with a Nikon D80 camera adapted with an NIR infrared sensor and a Nikon AF-S DX NIKKOR 18–135 mm 1:3.5-5.6G ED camera lens.

Powder X-ray diffraction (PXRD)

Powder X-ray diffraction (PXRD) patterns were collected on a Rigaku MiniFlex 6G equipped with a Cu-target (λ = 1.54 Å) sealed-tube X-ray source operating at 40 kV/15 mA and a D/teX.

Results and discussion

The Box–Behnken design was constructed by selecting time, temperature, and OAm/Oa volume as primary variables, as seen in Fig. 1b. This yielded 15 reactions, including three centre-point reactions to assess variability in the analysis as observed in Table S2. Fig. 2 shows the TEM micrographs obtained from the Box–Behnken. As observed in the size histograms in Fig. S1, we noticed factors like temperature have a remarkable effect on NPs average size, as NPs prepared at the highest temperature condition (240 °C), cause the largest distribution of particles, while the lowest temperature conditions (200 °C) show smaller NPs. From the ANOVA table, it can be noted that temperature, time, and ligand concentration have a statistically significant effect on the NPs average size, as their p-values are below 0.001. Of these three factors, temperature is the most influential variable (F = 280.8), followed by time (F = 63.4) and lastly ligand composition (F = 48.2). Quadratic effects for the temperature, time, and ligand composition are above a p-value of 0.05, showing that the response is linear mainly in the selected ranges of the experiment.

Two-variable interactions suggest that the effect between temperature and ligand composition has a significant impact on defining NPs average size (p = 0.012), and the same can be inferred from the interaction between time and ligand composition (p = 0.02). The interaction between temperature and time did not show a statistically significant effect on average size (p = 0.063). This may be due to insufficient curvature in the response surface, as both factors appear to influence average size in a similar proportional manner. Their combined effect does not amplify or diminish size growth, rendering the interaction negligible. The lack of fit test yielded a p-value of 0.3817, rendering it insignificant, showing that the model ade-

Table 1 ANOVA table and model statistics obtained for fitting a full quadratic model with a confidence value of 95%

| ANOVA						Model statistics	
	DF	Sum of squares	Mean square	F Value	Prob > F		Size
Temperature	1	61.938	61.938	280.806	1.38×10^{-5}	Degrees of freedom	5
Time	1	13.992	13.992	63.434	5.03×10^{-4}	Root mean square of error	0.469
Ligand composition	1	10.626	10.626	48.174	9.53×10^{-4}	R-Square	0.988
Temperature × temperature	1	6.16×10^{-4}	6.16×10^{-4}	0.002	0.959	Adj. R-square	0.967
Time × time	1	0.990	0.990	4.490	0.087	Press	13.486
Ligand composition × ligand composition	1	0.692	0.692	3.137	0.136	Residual sums of squares	1.102
Temperature × time	1	1.243	1.243	5.636	0.063	Predicted. R-Square	0.859
Temperature × ligand composition	1	3.186	3.183	14.445	0.012		
Time × ligand composition	1	2.205	2.205	9.997	0.025		
Error	5	1.102	0.220				
Lack of fit	3	0.800	0.266	1.764	0.381		
Pure error	2	0.302	0.151				
Total	14	95.869					
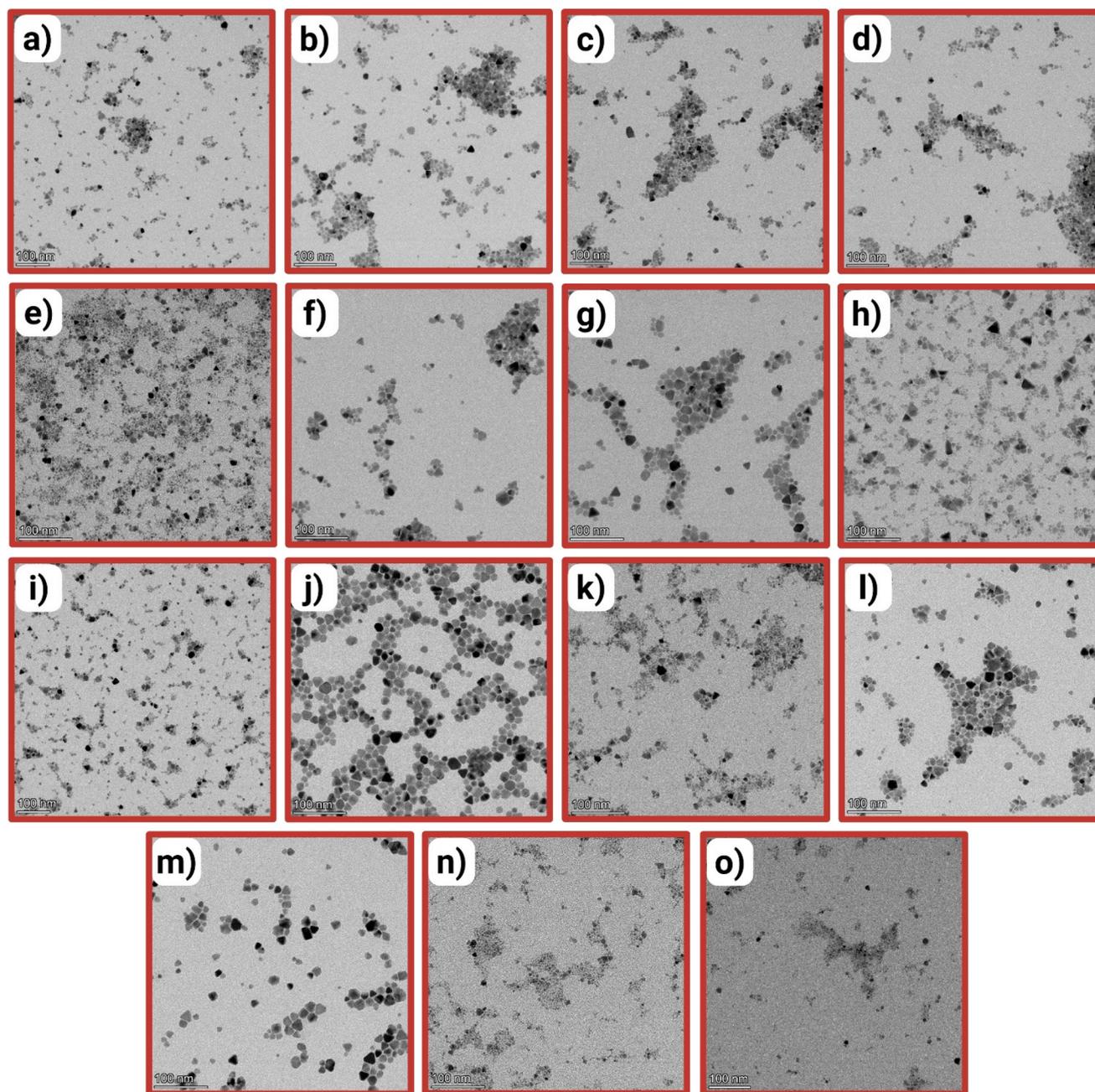
Fig. 2 TEM micrographs with a 100 nm bar scale of (a) 220 °C, 17.5 min, 2/2, (b) 220 °C, 30 min, 3/1, (c) 220 °C, 17.5 min, 2/2, (d) 220 °C, 17.5 min, 2/2, (e) 200 °C, 17.5 min, 1/3, (f) 200 °C, 17.5 min, 3/1, (g) 240 °C, 17.5 min, 3/1, (h) 220 °C, 30 min, 1/3, (i) 220 °C, 5 min, 3/1, (j) 220 °C, 5 min, 1/3, (k) 240 °C, 17.5 min, 1/3, (l) 200 °C, 30 min, 2/2, (m) 240 °C, 5 min, 2/2, (n) 240 °C, 30 min, 2/2, (o) 200 °C, 5 min, 2/2.

quately fits the experimental data. To quantify the impact of each synthesis parameter, the percentage contribution of each variable was determined based on the sum of squares from the ANOVA results (Table S3). Temperature was identified as the most influential variable, accounting for 65.29% of the total effect on average NPs size. Reaction time and ligand composition followed with contributions of 14.75% and 11.20%, respectively. Regarding significant interactions, the temperature × ligand composition contributed to 3.36% and time ×

ligand composition to 2.32% terms also exerted a measurable influence on the growth process. These results reveal that average size is mostly influenced by the applied thermal energy for NPs synthesis, leaving the rest of significant variables and their interactions to a low level of influence on the system mostly below 15%.

Model statistics also provide favourable results with an R^2 value of 0.9885, showing that the model explains nearly 99% of the variability. The adjusted R^2 with a value of 0.9677 shows

the terms are meaningful and do not overfit the data. Root-mean-square error remains small compared to the size of the response, showing low residual variability. The residual sum of squares is low compared to the total sum of squares, showing that the model explains 1.15% of the variation. Finally, the predicted R-squared suggests the model can explain 85.9% of the observed size variation. Residual analysis enables the evaluation of hidden variables that may affect the accuracy of the model. In the residuals *vs.* row order plot (Fig. S2a), the points appear randomly distributed with no clear trend or systematic deviation, suggesting a good fit. However, some clustering may show the influence of external factors such as manipulation consistency or batch effects, which could cause drift in experimental values. This is consistent with the model's ability to predict approximately 84% of the observed values. The residual *vs.* fitted Y (Fig. S2b) also shows equal scattering across positive and negative values, with a slight tendency for positive residuals at mid-range and negative one at higher values, showing a small effect of non-linearity not fully captured by the model. Neither residual invalidates the model, as no clear tendency in the residual position is seen. The normal probability (Fig. S2c) plot shows the residual points distributed across the fitted line, assuming a good level of normality across the sample distribution; however, slight deviations can be found at the extremes. Overall, the data show a good fit, showing that the model results can be primarily associated with the effect of the three main tested variables.

Proceeding with the analysis of the main factor interactions in Fig. 3a–c, it can be observed that there is a positive linear effect in average size increase as temperature increases from 200 to 240 °C, an effect commonly observed during the initial stages of NPs nucleation.[35] In agreement with the variable percentage of contributions, temperature was the factor that induced the biggest spread in NPs average size among the conditions tested having a contribution of 65.2%. This was followed by time (Fig. 3b) which also showed an increase in the observed average NPs although having a lower contribution (14.75%). However, the rate of increase reduces as the synthesis approaches 30 min, suggesting a growth saturation point that can be related to processes, such as surface depletion and reduction in the available precursor for nucleation.[35] Ligand composition, on the other hand, suggests that an increase of OAm content during synthesis leads to a decrease in the average size of the ensemble of NPs. Other reports have shown that higher Oa/OAm ratios lead to a high concentration of RCOO$^-$ species that form stable complex species with lower nucleation rates, thus promoting larger NPs forming over smaller nuclei.[36] While others show Oa can decrease precursor reactivity, maintaining unreacted precursors for a longer period, promoting the formation of larger NPs.[37] Variation in average NP size depending on the OAm and Oa ratio has also been observed in other types of NPs, such as Au and iron oxide NPs, where an increasing Oa to OAm ratio increased the average NP size.[36,38–41] To further prove this effect, reaction controls were conducted in which reactions at 220 °C, 17 min were conducted in the presence of

only OAm and Oa. TEM micrographs and histograms presented in Fig. S3a–c again show that the prominent presence of Oa leads to a larger average size of the ensemble compared to reactions involving higher quantities of OAm.

The two-way interactions of variables can be seen in Fig. 3d–f. The interaction between temperature and time (Fig. 3d) shows that the slopes across different time points are similar, suggesting that the effect of temperature is additive and does not alter the growth trend. This observation aligns with the ANOVA results, which did not identify a statistically significant interaction between these two variables in the model. Knowing that higher contents of OAm result in a reduction of the average NPs size the interaction of time and ligand composition, as observed in Fig. 3e, higher amounts of OAm aids in the reduction of average size increase over the range of time analysed, which could be related to the slow release of precursor for NPs formation. Conversely, increasing the concentration of Oa to OAm accelerates the growth rate, providing a larger and closely linear increase of the NPs average size. By visualising the interaction plot of temperature and ligand composition, it can be observed that at low temperatures, such as 200 °C, the average size of the NPs is not significantly affected, even in OAm or Oa-rich conditions. Increasing the temperature to 220 °C aids in the reduction of the average NPs size at higher concentrations of OAm. In contrast, the highest temperature (240 °C) results in the most pronounced average size reduction of nearly 3 nm, between the conditions with the highest concentrations of OAm and Oa. This effect may be attributed to increased attachment of OAm to the NPs surface, which could hinder precursor diffusion into the NPs.

Fig. 3g shows the relationship between reaction temperature and ligand and its effect on average NPs size as seen through a surface plot. In this graph, distinct regions with the same colour show variable temperature and ligand ratio combinations that achieve the exact value of responses. As an example, an average size of ~12 nm can be achieved at conditions of ~220 °C with lower ligand composition (Oa-rich, ~1.0) and higher temperatures (~240 °C) with a higher content of OAm (~3.0). This overlap suggests that growth can be tuned by adjusting either the reaction temperature or the ligand composition, offering synthetic flexibility. Increasing temperature leads to larger particles across all ligand ratios, but the effect is more pronounced under Oa-rich conditions (~1.0) compared to OAm-rich conditions (~3.0), where particle growth is more limited, as stronger coordination from OAm stabilises the surface and suppresses average size increase even at higher temperatures. Fig. 3h presents the contour plot of the interaction of reaction time and ligand ratios on NPs average size. Like the behaviour seen with temperature, contour regions show overlapping conditions that result in the exact average sizes. Particles of ~11 nm are obtained both at shorter times (~10 min) with low ligand ratios (Oa-rich, ~1.0) and at longer times (~30 min) with OAm-rich conditions (~2.5). This again highlights that particle growth can be slowed, or accelerated, by tuning ligand composition, where it is clearer that Oa-rich
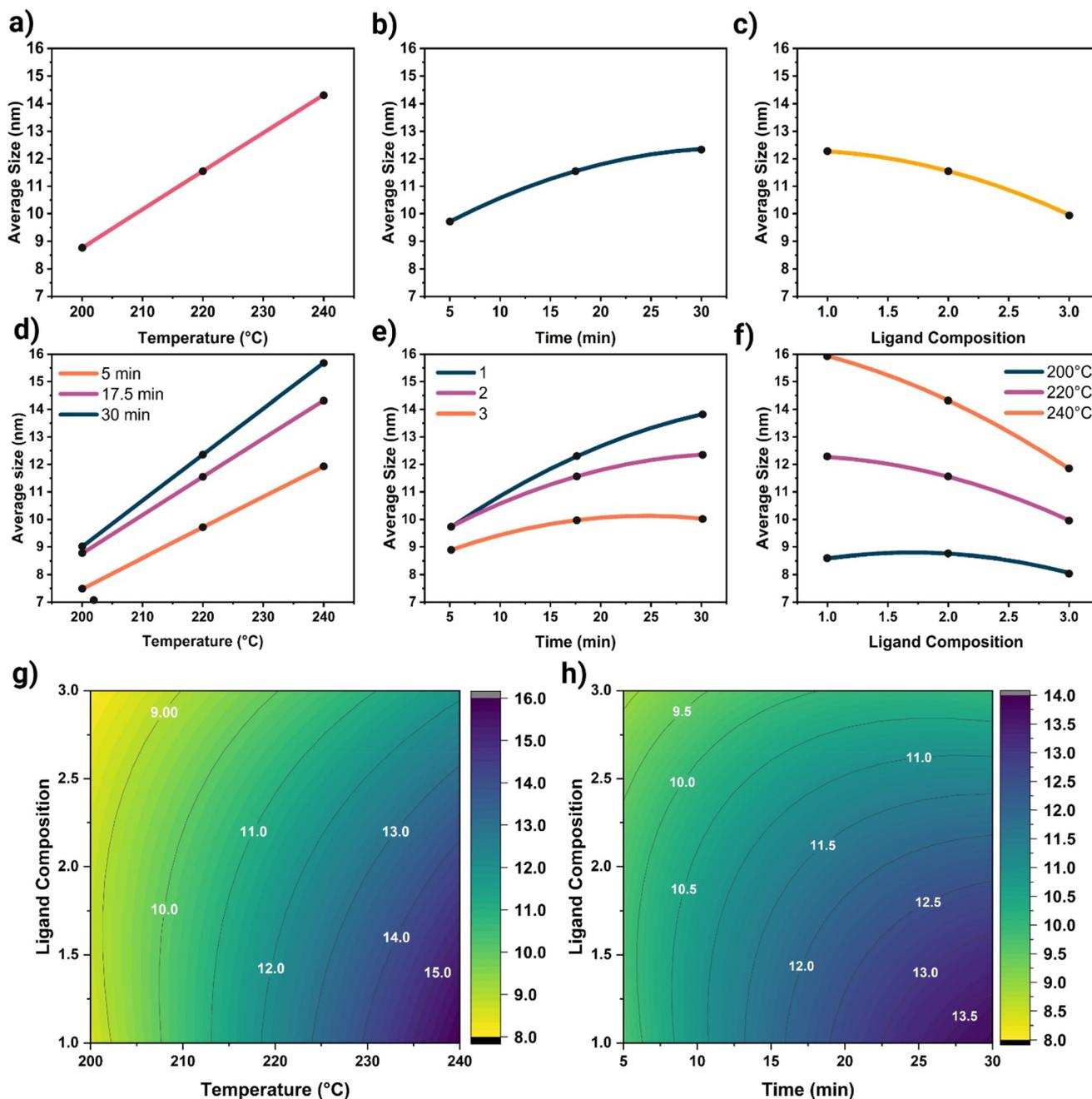
Fig. 3 RSA of CuInSe$_2$ nanoparticle size. (a–c) Main effects of temperature, reaction time, and ligand composition, showing that particle size increased strongly with temperature, rose moderately with time, and decreased with higher ligand composition. (d) Interaction of temperature and time, where size increased mainly with temperature, largely independent of time. (e) Interaction of time and ligand composition, where longer times and larger ligand quantities led to smaller sizes. (f) Interaction of ligand composition and temperature, where higher temperature dominated size increase despite ligand effects. (g) Contour plot of size *versus* temperature and ligand composition, highlighting the strong role of temperature. (h) Contour plot of size *versus* time and ligand composition, showing weaker dependence on time compared to ligand composition.

environments favour bigger NPs average sizes. Its growth is reduced even at low concentrations of OAm.

Powder X-ray diffraction (Fig. S4) confirmed the formation of purely CuInSe$_2$ chalcopyrite NPs at the range of temperature tested (2/2 ligand composition), with the appearance of 3 distinct Bragg reflections centered on 26°, 46°, and 55° 2θ, corres-

ponding to the Miller planes (112), (204), and (312), respectively (JCPDS 35-1102).[42] UV-Vis spectroscopy (Fig. S5) also corroborated CuInSe$_2$ by obtaining a featureless absorption spectrum characteristic of CuIn(S/Se)$_2$ NPs.[42] CuIn(S/Se)$_2$ NPs are well known for their intrinsically low quantum yield[2,5,43–45] which are commonly in the red to infrared region of the
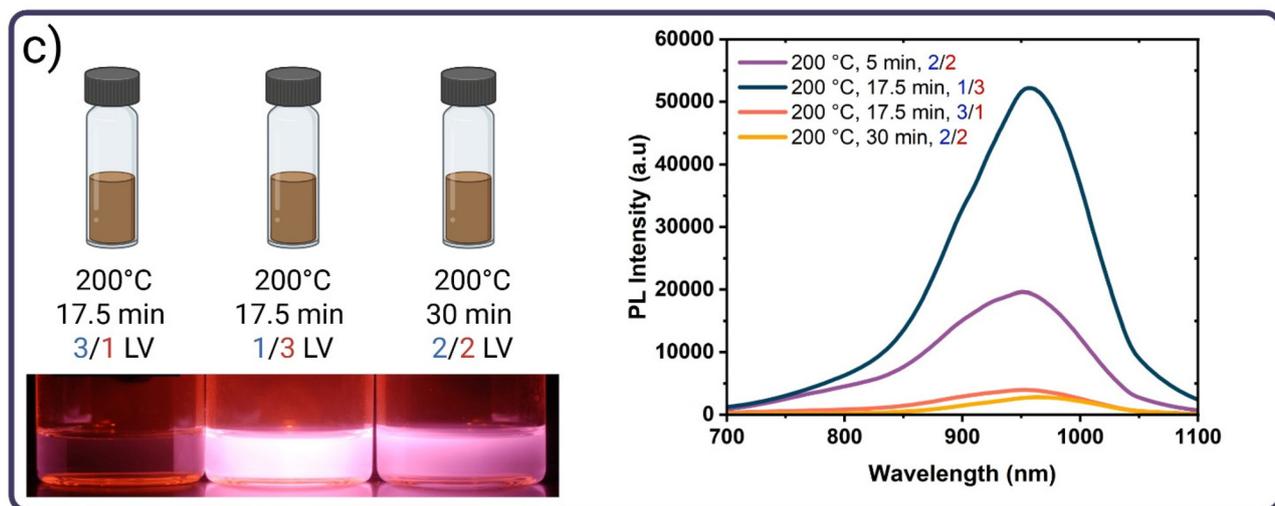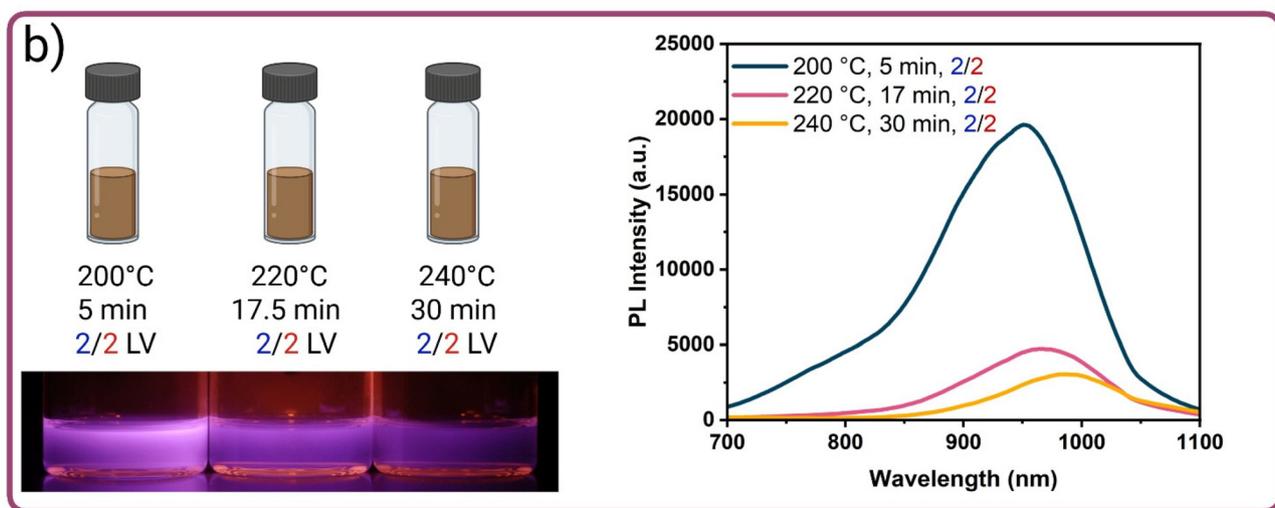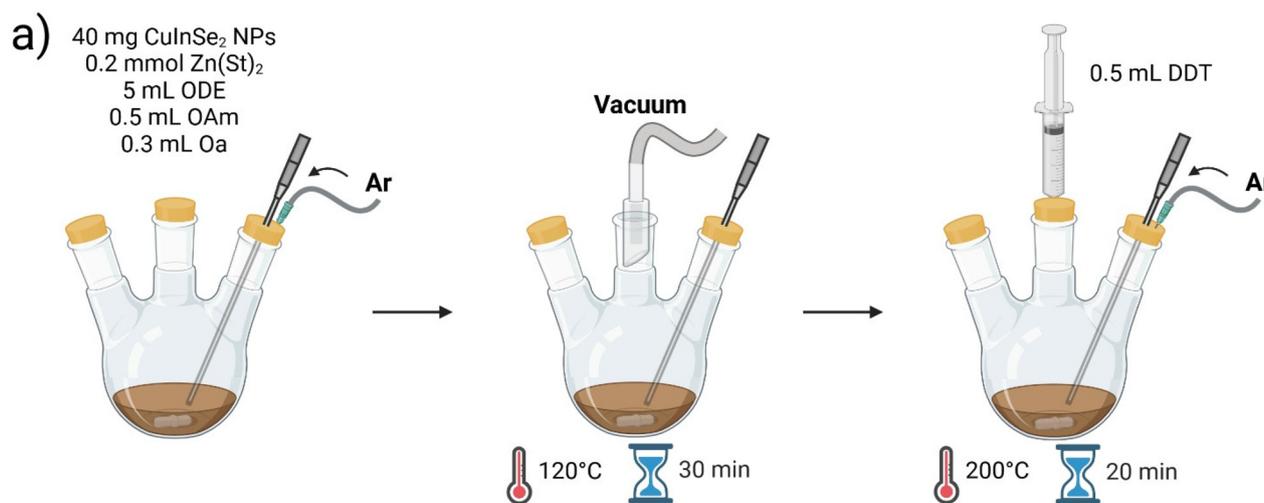
Fig. 4 (a) Schematic of CuInSe$_2$ nanoparticles with ZnS. (b) RSA sample selection for passivation studies, ligand quantity was fixed at the canter while varying time and temperature for the highest difference in size, the effect of temperature and reaction time on PL properties at a 2/2 ligand quantity was determined through IR (λ_{ex} = 365 nm) photography and PL, indicating that the sample heated at 200 °C showed the highest PL intensity (λ_{ex} = 365 nm). (c) 200 °C RSA sample survey, passivation with ZnS caused an increase in PL for all the samples sharing 200 °C as the common variable, samples with 17.5 min and 1/3 showed the highest increase in PL compared to the rest of the conditions sharing 200 °C as the temperature value.

spectrum.[43,44,46] In order to enhance PL properties, approaches such as Zn alloying or ZnS surface passivation have been shown to effectively enhance properties such as emission.[43,44,47,48] Because of such low optical properties of the base material, it poses challenges when evaluating synthesis outcomes through DOE or RSA, as in several cases, the analysis of PL signal for the conditions created by the Box–Behnken design leads to the absence of PL, or result in low emission intensity that would render the identification of the emission center unreliable, resulting in incomplete datasets for the optical responses. This limitation complicates the direct use of RSA to optimize PL properties. To address this issue, an indirect strategy was employed in which NPs average size was first used as the primary response in the RSA study. From the previous analysis, three representative conditions were selected to capture a basic range of NPs sizes: 200 °C, 5 min, 2/2 (small), 220 °C, 17.5 min, 2/2 (medium), and 240 °C, 30 min, 2/2 ratio (large). The selection of these conditions provides a rational basis for evaluating the influence of average size on the optical response following ZnS passivation.

The passivation procedure was carried out as shown in Fig. 4a. Passivation of these samples and further analysis through PL revealed that the 200 °C sample exhibited the strongest PL intensity after ZnS passivation (Fig. 4b), followed by samples prepared at 220 °C, 17.5 min, and 240 °C, 30 min. This result may suggest that lower reaction temperatures favour surfaces that are more reactive toward passivation precursors, through differences in OAm and Oa binding across the different temperatures. This can also be related to the formation of defects at higher reaction temperatures, which can cause reduced optical properties even after ZnS passivation. The unique formation of a passivation layer with the absence of secondary binary structures, such as ZnS, was then evaluated through PXRD (Fig. S6), which shows the chalcopyrite phase. This is further supported by the UV-Vis spectra, which showed a featureless spectrum expected from $CuInSe_2$ samples (Fig. S7). Guided by these findings, a new sample selection was conducted on all synthesis conditions at 200 °C with varying ligand ratios and reaction times: 200 °C, 17.5 min, 3/1, 200 °C, 17.5 min, 1/3, and 200 °C, 30 min, 2/2. Among these, the Oa-rich environment yielded the highest PL intensity following ZnS passivation (Fig. 4c), followed by the previously selected condition in the initial survey (200 °C, 5 min, 2/2), then 200 °C, 17.5, 3/1, and 200 °C, 30 min, 2/2, which all achieved a close PL intensity. The previous observation highlights the importance of ligand composition in controlling surface chemistry. Although the difference in passivation between surfaces covered with amine-type ligands and carboxylic acid ligands has not been directly addressed in $CuInS_2$, other studies have found differences in the PL properties following passivation with different carboxylic acid structures, such as ethylhexanoic acid, which proved more effective in passivation compared to Oa.[49] In other instances, OAm has proven to produce NPs with lower PL properties compared to other ligands such as diphenylphosphine and ODE,[8] or hexanethiol.[13]

To our knowledge, the difference in PL properties through passivation in surfaces rich in Oam-rich and Oa-rich surfaces has not been addressed in $CuIn(S/Se)_2$ NPs. However, other reports have explained the importance of organic washing residues on the surface of $CuInS_2$, where acetone residues aided in the epitaxial growth of ZnS rather than alloying or etching. Although ZnS has better growth, this is not reflected in the formation of NPs with higher PL properties, showing the participation of other factors in defining the outcomes in PL properties.[50]

Conclusions

Our findings show RSA offers clear advantages in statistically analysing key aspects of nanoparticle synthesis and design. It enables both modeling of the synthesis process and accurate evaluation of the interactions and individual effects of standard variables involved in nanoparticle formation. From this work, it can be concluded that, within the tested ranges and conditions, variables such as time and temperature increase nanoparticle average size; however, this increase may be associated with phenomena such as monomer depletion during nucleation, which affects growth dynamics. This is reflected in the time factor, where at longer durations, the nanoparticle growth rate decreases.

Another important factor is the composition of the selected ligands. It was observed that oleylamine-rich conditions promote the formation of smaller particles, whereas oleic-acid-rich conditions favor larger ones. This effect is further influenced by interactions among variables such as time and temperature, which affect the magnitude of average size increase or decrease. Although each condition may yield different outcomes, surface plots allow identification of common regions where similar response values can be obtained. This is useful when specific temperatures, times, or ligand composition must be avoided.

While RSA proved to be an effective tool for analyzing the average nanoparticle average size, the analysis of other responses, such as PL, depends strongly on the nature of the sample. This renders interpretation especially complex for materials with low PL quantum yields, such as $CuInSe_2$. The detailed analysis provided by RSA allowed an introductory survey among the samples produced to identify compositions whose characteristics favor better defect passivation by ZnS, leading to improved optical properties. From this, it was found that samples synthesized at lower temperatures, which were correlated with smaller average particle sizes, showed higher emission intensities compared to those obtained at higher temperatures and longer times. The comparison among samples synthesized at 200 °C showed that, besides low temperature and short time, ligand composition also played a significant role in passivation. In particular, oleic-acid-rich conditions resulted in the highest emission intensity. Future work should build on these findings by exploring how surface passivation strategies, such as ZnS coating, can be tuned to further

enhance the optical and electronic properties of CuInSe$_2$ nanostructures. A deeper understanding of how synthesis parameters couple with passivation efficiency will be key to advancing these materials toward practical optoelectronic applications.

Author contributions

L. P.: conceptualization, methodology, investigation, formal analysis, writing – original draft, writing – review and editing; C. H.: conceptualization, methodology, investigation, formal analysis, writing – review and editing; J. A. C and R. N.: conceptualization, methodology, resources, writing – review and editing, supervision, and funding acquisition.

Conflicts of interest

The authors declare no conflict of interest.

Data availability

The authors confirm that the data supporting the findings of this manuscript are available within the article and its supplementary information (SI). Supplementary information: TEM particle size histograms, particle size statistics, UV-Vis of synthesized samples, model residuals figures, UV-Vis of passivated samples, PXRD of passivated samples. HAADF-STEM EDX mapping of passivated sample. See DOI: https://doi.org/10.1039/d5nr04926a.

Acknowledgements

References

1 C. Coughlan, M. Ibáñez, O. Dobrozhan, A. Singh, A. Cabot and K. M. Ryan, *Chem. Rev.*, 2017, **117**, 5865–6109.

2 W. Lian, D. Tu, P. Hu, X. Song, Z. Gong, T. Chen, J. Song, Z. Chen and X. Chen, *Nano Today*, 2020, **35**, 100943.

3 R. Adel, S. Ebrahim, A. Shokry, M. Soliman and M. Khalil, *ACS Omega*, 2021, **6**, 2167–2176.

4 S. Qu, X. Yuan, Y. Li, X. Li, X. Zhou, X. Xue, K. Zhang, J. Xu and C. Yuan, *Nanoscale Adv.*, 2021, **3**, 2334–2342.

5 C. Xia, W. Wu, T. Yu, X. Xie, C. van Oversteeg, H. C. Gerritsen and C. de Mello Donega, *ACS Nano*, 2018, **12**, 8350–8361.

6 B. Zu, S. Chen, Q. Jin, Z. Xu, X. Wu and L. Wu, *Inorg. Chem.*, 2024, **63**, 21816–21821.

7 X. Zhao, Y. Huang and J. F. Corrigan, *Inorg. Chem.*, 2016, **55**, 10810–10817.

8 G. Wang, H. Wei, J. Shi, Y. Xu, H. Wu, Y. Luo, D. Li and Q. Meng, *Nano Energy*, 2017, **35**, 17–25.

9 L. Páramo, M. Pains Duarte, G. Fuoco, A. Adedapo, D. P. Singh and R. Naccache, *J. Mater. Chem. A*, 2025, **13**, 28819–28844.

10 V. Perner, T. Rath, F. Pirolt, O. Glatter, K. Wewerka, I. Letofsky-Papst, P. Zach, M. Hobisch, B. Kunert and G. Trimmel, *New J. Chem.*, 2019, **43**, 356–363.

11 B. A. Tappan, G. Barim, J. C. Kwok and R. L. Brutchey, *Chem. Mater.*, 2018, **30**, 5704–5713.

12 C. Xia, P. Tamarat, L. Hou, S. Busatto, J. D. Meeldijk, C. De Mello Donega and B. Lounis, *ACS Nano*, 2021, **15**, 17573–17581.

13 J. Du, R. Singh, I. Fedin, A. S. Fuhr and V. I. Klimov, *Nat. Energy*, 2020, **5**, 409–417.

14 S. M. Harvey, D. W. Houck, W. Liu, Y. Liu, D. J. Gosztola, B. A. Korgel, M. R. Wasielewski and R. D. Schaller, *ACS Nano*, 2021, **15**, 19588–19599.

15 M. Gromova, A. Lefrançois, L. Vaure, F. Agnese, D. Aldakov, A. Maurice, D. Djurado, C. Lebrun, A. de Geyer, T. U. Schülli, S. Pouget and P. Reiss, *J. Am. Chem. Soc.*, 2017, **139**, 15748–15759.

16 E. A. Hernández-Pagán, A. D. P. Leach, J. M. Rhodes, S. Sarkar and J. E. Macdonald, *Chem. Mater.*, 2015, **27**, 7969–7976.

17 H. Zhong, Z. Wang, E. Bovero, Z. Lu, F. C. J. M. van Veggel and G. D. Scholes, *J. Phys. Chem. C*, 2011, **115**, 12396–12402.

18 N. Ntholeng, B. Mojela, S. Gqoba, M. Airo, S. Govindraju, M. J. Moloto, J. Van Wyk and N. Moloto, *New J. Chem.*, 2016, **40**, 10259–10266.

19 A. Fuhr, H. J. Yun, S. A. Crooker and V. I. Klimov, *ACS Nano*, 2020, **14**, 2212–2223.

20 W. Van Der Stam, M. De Graaf, S. Gudjonsdottir, J. J. Geuchies, J. J. Dijkema, N. Kirkwood, W. H. Evers, A. Longo and A. J. Houtepen, *ACS Nano*, 2018, **12**, 11244–11253.

21 A. S. Fuhr, H. J. Yun, N. S. Makarov, H. Li, H. McDaniel and V. I. Klimov, *ACS Photonics*, 2017, **4**, 2425–2435.

22 A. C. Berends, F. T. Rabouw, F. C. M. Spoor, E. Bladt, F. C. Grozema, A. J. Houtepen, L. D. A. Siebbeles and C. De Mello Donegá, *J. Phys. Chem. Lett.*, 2016, **7**, 3503–3509.

23 L. R. Karadaghi, M. S. Madani, E. M. Williamson, A. T. To, S. E. Habas, F. G. Baddour, J. A. Schaidle, D. A. Ruddy, R. L. Brutchey and N. Malmstadt, *ACS Appl. Nano Mater.*, 2022, **5**, 1966–1975.

24 E. M. Williamson, B. A. Tappan, L. Mora-Tamez, G. Barim and R. L. Brutchey, *ACS Nano*, 2021, **15**, 9422–9433.

25 R. W. Baker, L. Forfar, X. Liang and P. J. Cameron, *React. Chem. Eng.*, 2021, **6**, 709–719.

26 L. Mora-Tamez, G. Barim, C. Downes, E. M. Williamson, S. E. Habas and R. L. Brutchey, *Chem. Mater.*, 2019, **31**, 1552–1560.

27 E. M. Williamson, Z. Sun, L. Mora-Tamez and R. L. Brutchey, *Chem. Mater.*, 2022, **34**, 9823–9835.

28 I. Alkian, H. Sutanto and Hadiyanto, *Mater. Res. Express*, 2022, **9**, 015702.

29 E. Zanda, A. Irto, S. G. M. Raccuia, C. Bretti, G. De Luca, I. Ielo, M. Zoccali, A. Arena, G. Paladini, F. Caridi, M. Formica, E. Macedi, V. Venuti, C. De Stefano, L. Mondello, P. Cardiano and G. Lando, *J. Environ. Chem. Eng.*, 2025, **13**, 118472.

30 J. Billet, W. Dujardin, K. De Keukeleere, K. De Buysser, J. De Roo and I. Van Driessche, *Chem. Mater.*, 2018, **30**, 4298–4306.

31 A. Di Tocco, G. V. Porcal, W. I. Riberi, M. A. Zon, H. Fernández, S. N. Robledo and F. J. Arévalo, *New J. Chem.*, 2019, **43**, 12836–12845.

32 F. Baum, T. Pretto, R. A. Gouvêa and M. J. L. Santos, *Cryst. Growth Des.*, 2022, **22**, 3669–3679.

33 X. Zhang, X. Zhang, T. R. Graham, C. I. Pearce, B. L. Mehdi, A. T. N'Diaye, S. Kerisit, N. D. Browning, S. B. Clark and K. M. Rosso, *Cryst. Growth Des.*, 2017, **17**, 6801–6808.

34 Ch. Barglik-Chory, Ch. Remenyi, H. Strohm and G. Müller, *J. Phys. Chem. B*, 2004, **108**, 7637–7640.

35 N. T. K. Thanh, N. Maclean and S. Mahiddine, *Chem. Rev.*, 2014, **114**, 7610–7630.

36 H. Sharifi Dehsari, R. A. Harris, A. H. Ribeiro, W. Tremel and K. Asadi, *Langmuir*, 2018, **34**, 6582–6590.

37 S. Mourdikoudis, M. Menelaou, N. Fiuza-Maneiro, G. Zheng, S. Wei, J. Pérez-Juste, L. Polavarapu and Z. Sofer, *Nanoscale Horiz.*, 2022, **7**, 941–1015.

38 D. Dadarlat, I. Craciunescu, R. Turcu and C. Tripon, *Int. J. Thermophys.*, 2017, **38**, 86.

39 M. B. Mohamed, K. M. AbouZeid, V. Abdelsayed, A. A. Aljarash and M. S. El-Shall, *ACS Nano*, 2010, **4**, 2766–2772.

40 N. V. Pul'kova, S. A. Tonevitskaya, V. M. Gerasimov, P. G. Rudakovskaya, A. G. Mazhuga and D. A. Sakharov, *Nanotechnol. Russ.*, 2015, **10**, 570–575.

41 J. Mohapatra, F. Zeng, K. Elkins, M. Xing, M. Ghimire, S. Yoon, S. R. Mishra and J. P. Liu, *Phys. Chem. Chem. Phys.*, 2018, **20**, 12879–12887.

42 W. P. R. Liyanage and M. Nath, *Sci. Rep.*, 2019, **9**, 16751.

43 Z. Liu, C. Hao, Y. Sun, J. Wang, L. Dube, M. Chen, W. Dang, J. Hu, X. Li and O. Chen, *Nano Lett.*, 2024, **24**, 5342–5350.

44 J. Ning, Y. Xiong, F. Huang, Z. Duan, S. V. Kershaw and A. L. Rogach, *Chem. Mater.*, 2020, **32**, 7842–7849.

45 J. Ning, Z. Duan, S. V. Kershaw and A. L. Rogach, *ACS Nano*, 2020, **14**, 11799–11808.

46 E. Cassette, T. Pons, C. Bouet, M. Helle, L. Bezdetnaya, F. Marchal and B. Dubertret, *Chem. Mater.*, 2010, **22**, 6117–6124.

47 S. Yamashita, M. Tanabe, T. Araki, M. Shiomi, T. Nishi and Y. Kudo, *J. Phys. Chem. C*, 2022, **126**, 14558–14565.

48 C. Xia, N. Winckelmans, P. T. Prins, S. Bals, H. C. Gerritsen and C. de Mello Donegá, *J. Am. Chem. Soc.*, 2018, **140**, 5755–5763.

49 S. Zang, X. Zhang, Y. Sun, N. Li, L. Wang and L. Li, *Frontiers in Chemistry*, 2022, **10**, DOI: 10.3389/fchem.2022.1102514.

50 A. C. Berends, W. van der Stam, J. P. Hofmann, E. Bladt, J. D. Meeldijk, S. Bals and C. de Mello Donega, *Chem. Mater.*, 2018, **30**, 2400–2413.